# Molecular Simulations of Solved Co-crystallized X-Ray Structures Identify Action Mechanisms of PDEδ Inhibitors

**ARTICLE** *in* BIOPHYSICAL JOURNAL · AUGUST 2015

Impact Factor: 3.97 · DOI: 10.1016/j.bpj.2015.08.001



**5 AUTHORS**, INCLUDING:

Ramin Ekhteiari Salmas

Istanbul Technical University

**18** PUBLICATIONS **20** CITATIONS

SEE PROFILE

Mine Yurtsever

Istanbul Technical University

**59** PUBLICATIONS **349** CITATIONS

SEE PROFILE

Sergei Y Noskov

The University of Calgary

**131** PUBLICATIONS **2,112** CITATIONS

SEE PROFILE

Serdar Durdagi

Bahçeşehir University

**81** PUBLICATIONS **836** CITATIONS

SEE PROFILE

Article

# Molecular Simulations of Solved Co-crystallized X-Ray Structures Identify Action Mechanisms of PDEδ Inhibitors

Ramin Ekhteiari Salmas,[1] Mert Mestanoglu,[2] Mine Yurtsever,[1] Sergei Y. Noskov,[3] and Serdar Durdagi[4,*]
[1]Department of Chemistry, Istanbul Technical University, Istanbul, Turkey; [2]School of Medicine, Bahcesehir University, Istanbul, Turkey; [3]Centre for Molecular Simulation, Department of Biological Sciences, University of Calgary, Calgary, Alberta, Canada; and [4]Department of Biophysics, School of Medicine, Bahcesehir University, Istanbul, Turkey

ABSTRACT PDEδ is a small protein that binds and controls the trafficking of RAS subfamily proteins. Its inhibition protects initiation of RAS signaling, and it is one of the common targets considered for oncological drug development. In this study, we used solved x-ray structures of inhibitor-bound PDEδ targets to investigate mechanisms of action of six independent all-atom MD simulations. An analysis of atomic simulations combined with the molecular mechanic-Poisson-Boltzmann solvent accessible surface area/generalized Born solvent accessible surface area calculations led to the identification of action mechanisms for a panel of novel PDEδ inhibitors. To the best of our knowledge, this study is one of the first in silico investigations on co-crystallized PDEδ protein. A detailed atomic-scale understanding of the molecular mechanism of PDEδ inhibition may assist in the design of novel PDEδ inhibitors. One of the most common side effects for diverse small molecules/kinase inhibitors is their off-target interactions with cardiac ion channels and human-ether-a-go-go channel specifically. Thus, all of the studied PDEδ inhibitors are also screened in silico at the central cavities of hERG1 potassium channels.

## INTRODUCTION

RAS (rat sarcoma) superfamily members belong to the protein family of small GTPases. RAS regulates signaling networks and cell proliferation (1). Abnormal cell signaling, proliferation, and mutation of proto-oncogenes are known to occur in cancer cells (2,3). RAS mutations are involved in ~30% of all human cancers, rendering this oncogene as one of the major targets in anticancer drug development (4). The three well-defined subfamilies of RAS proteins are Harvey rat sarcoma viral oncogene homolog (H-RAS), Kirsten rat sarcoma 2 viral oncogene homolog (K-RAS), and neuroblastoma RAS viral oncogene homolog (N-RAS) (5,6). RAS proteins are composed of 189 amino acid residues with the first 85 amino acids strictly conserved among family members (7). In the mostly observed human cancer types, such as colon, lung, and pancreatic, mutations of RAS genes have been observed (8). The K-RAS consists of two isoforms: K-RAS4A, which exists in the viral K-RAS oncogene and 4B preferably denoted in human cells (9,10); and K-RAS4B, which is the most important isoform of the RAS proteins, and which hold a central position in the transduction of growth-promoting signals across the plasma membrane to regulate cell growth and differentiation. Signaling activity of K-RAS is dependent on its enrichment level in the plasma membrane (PM). Moreover, PM specificity is related to the electrostatic interactions between PM and K-RAS (3). Recently, PM localization of RAS proteins is thought to be dependent on the PDEδ activity levels (7). Additionally, PDEδ regulates RAS activity and may suppress oncogenic RAS-related signaling in cells. Consequently, interfering with K-RAS signaling is significant to obtain useful anticancer drugs. In recent studies, several benzimidazole compounds have been found to be good inhibitors of the KRAS-PDEδ communication (11). These small molecules bind selectively to the binding pocket of PDEδ to inhibit oncogenic signaling of K-RAS. This inhibition suppresses cancer cell proliferation and tumor growth.

## MATERIALS AND METHODS

### Protein preparation process

In this study, co-crystallized PDEδ complexes were retrieved from Protein Data Bank (PDB ID: 4JV6, 4JV8, 4JVB, 4JVF) (11) and their coordinates were used as the initial inputs for independent molecular dynamics (MD) simulations. Missing amino acid residues at the crystal structures were identified and predictively modeled using implemented MODELER 9.12 code (12) in UCSF Chimera (13) based on the amino acid sequence of PDEδ that was retrieved from the UniProt Knowledgebase (UniProtKB) server (14) (ID: O43924). Missing hydrogen atoms were then added, and the protonation properties of the proteins were assigned in the physiological pH (pH: 7.4) by utilizing the implemented PROPKA module (15) in the protein preparation wizard of the Maestro molecular modeling package (16). Finally all atoms of the systems were submitted in restrained molecular mechanics (MM) minimizations by employing the OPLS2005 force field. Complexes (PDB ID: 4JV6 and 4JV8) contain ligands **1** and **S1** in two domains of the binding pocket, respectively. These binding sites are identified by Tyr149 and Arg61 amino acid residues as critical key residues in each domain. Systems were constructed for each complex individually, with six systems in total elucidated (detailed in Results and Discussion).

*Submitted February 20, 2015, and accepted for publication August 3, 2015.*

*Correspondence: serdar.durdagi@bahcesehir.edu.tr

Editor: Randall Rasmusson



0006-3495/15/09/1163/6

http://dx.doi.org/10.1016/j.bpj.2015.08.001

## MD simulations

In our study two MD simulation programs (NAMD and AMBER) were used for different postprocessing analyses.

### *NAMD simulations*

Before independent MD simulations, each structure was solvated with TIP3P water molecules using 15 Å solvent layers around the protein complexes surface, and simulations were performed with NAMD 2.9 code (17) (see Fig. S1 in the Supporting Material).

The neutralizing counterions were added to represent physiological concentration of 0.15 M KCl. The CHARMM 36 and CHARMM general force field (CgenFF) (18,19) force fields were used to represent the protein-ligand systems. Heavy atom bond lengths with hydrogen atoms and the internal geometry of water molecules were fixed using the SHAKE algorithm. The simulations were run under periodic boundary conditions (PBC) with a 12 Å cut-off for nonbonding interactions. The particle mesh Ewald (PME) method was used to treat long-range electrostatic interactions. Before starting the MD production run, a two-equilibration stage was used: 1) the protein-ligand atoms were fixed, and the water molecules were allowed to relax for 1 ns and 2) all atoms were relaxed with a 1 ns equilibration run. Finally, 70 ns MD simulations (as production run) at constant pressure (1 atm) and temperature (300 K) were performed at the canonical ensemble for each systems. For all MD simulations, a time step of 2 fs was used. Trajectory frames were generated for every 10 ps for a total of 70 ns. All of the MD frames were analyzed using the modules with the VMD program package (20).

### *AMBER simulations*

To apply Poisson-Boltzmann (PB) solvent accessible surface area/generalized Born (GB) solvent accessible surface area (PBSA/GBSA) methods, independent MD simulations were individually performed for each of the complexes. Constructed and repaired systems (see the protein preparation section) were incorporated in these MD simulations. AMBER 12 code (21) was used for all classical MD simulations. The AMBER ff99SB force field (22) was utilized for atomic partial charges and bond, angle, dihedral, and van der Waals parameters were used for all atoms of proteins. Parameter data of proteins were constructed using the tLEaP module of AMBERTOOLS 13. The ANTECHAMBER module was employed to use the Gasteiger atomic partial charges individually for each of the inhibitors, and the general AMBER GAFF force field (23) was used to prepare the force field parameters. The systems were neutralized in tLEaP with $Na^+$ counterions and solvated with the explicit solvation method that is represented by TIP3P water model. Long-range electrostatic interactions were calculated using the PME method. All of the systems were simulated at the temperature of 300 K and the pressure of 1 atm for total of 50 ns production run. A time step of 2 fs was used for all MD simulations. Minimization and equilibration processes were then carried out to derive initial coordination for each studied system.

## Nonbonding interaction energy estimations

To understand the role of individual amino acids in the active sites of PDE$\delta$ complexes, each complex was submitted in nonbonding interaction energy calculations. To accomplish this, all amino acid residues within 6 Å from ligand were considered and their nonbonding energy values between ligand and amino acid residues were calculated using the NAMD energy plugin in VMD (20). Interaction energy values were estimated as follows:

$$\Delta E_{non-bonding} = E_{complex} - \left(E_{protein} + E_{ligand}\right). \quad (1)$$

These calculations were carried out using all generated MD trajectory frames and the average values of estimated interaction energy were considered. The implicit solvation method was employed for MM calculations.

## MM-PBSA/GBSA binding free energy calculations

Binding free-energy predictions have proven to be useful methods for many subjects in molecular modeling studies of biology systems, such as protein-ligand interactions, drug screening, and drug discovery (24). MM-PBSA/GBSA is a modern method that calculates the binding free energies of the complex (protein + ligand) systems based on MD simulations (24).

The free energy of binding can be described as a composition of enthalpy and entropy as follows:

$$\Delta G_{bind} = \Delta H - T\Delta S \quad (2)$$

$\Delta$H in Eq. 2 can be shown as follows:

$$\Delta H = \Delta E_{MM} + \Delta G_{sol}, \quad (3)$$

where $\Delta E_{MM}$ describes the molecular mechanics interaction energy between the receptor and the inhibitor, and $\Delta G_{sol}$ is the solvation free energy. $\Delta E_{MM}$ is expressed as follows (4):

$$\Delta E_{MM} = \Delta E_{elec} + \Delta E_{vdW}, \quad (4)$$

where each of the $\Delta E_{elec}$ and $\Delta E_{vdW}$ defines electrostatic interaction energy and van der Waals interaction energy, respectively. $\Delta G_{sol}$ is further divided as follows:

$$\Delta G_{sol} = \Delta G_{PB/GB} + \Delta G_{NP}, \quad (5)$$

where $\Delta G_{PB/GB}$ defines the polar solvation energy calculated by PB and GB methods using the PBSA module of AMBER 12. $\Delta G_{NP}$ describes nonpolar solvation energy that is predicted through estimation of the solvent-accessible surface area (SASA) as follows:

$$\Delta G_{NP} = \gamma SASA + \beta, \quad (6)$$

where the surface tension ($\gamma$) and the offset ($\beta$) was set the standard values of 0.005420 kcal mol$^{-1}$ Å$^{-2}$ and $-1.008000$ kcal mol$^{-1}$, respectively. $\Delta G_{NP}$ was estimated with the linear combinations of the pairwise overlaps (LCPO) method (25). In SASA calculation, a probe radius of 1.4 Å was assigned for the solvent. MMPBSA.py is a program written in Python and nab. In this study, both the PB and GB methods were considered for the calculation of binding free energies. MMPBSA.py, Python, and the nab-scripted program of AMBER 12 was utilized to perform these energetic calculations. One thousand trajectory frames from 50 ns MD simulations were submitted for each of the postprocessing binding free-energy calculations.

## Docking simulations

PDE$\delta$ inhibitors, as with many other anticancer drugs, display various side effects related to off-target interactions with cardiac channels, and most notably with the hERG1 channel (26). The Glide/XP (extra precision) docking method (27) was used to estimate the binding energy values between the inhibitors and hERG1 channels. Predicted open active and open-inactive hERG1 models from our earlier study (28) were used as receptor targets. Docking grids were identified for both models by utilizing the positions of Tyr652, Phe565, Ser649, Thr623, and Ser624 amino acid residues, and then all inhibitors were docked into the active sites of hERG1 channel models.

## RESULTS AND DISCUSSION

The x-ray structures provided an in-depth view of the potential organization of the binding pocket and key ligating

properties of the site. However, the receptor flexibility allowing specificity in ligand recognition often is a critical factor in the protein-ligand association. Therefore, there is an apparent need to understand conformational ensembles responsible for high affinity and high specificity of the receptor binding sites. One of the most popular approaches for this kind of problem is MD simulations. MD allows generation of the ensemble of structures that can be used for accurate computations of thermodynamics potentials such as binding free energies. The aim of this study was to investigate the binding mechanisms responsible for high-affinity binding for reported PDE$\delta$ inhibitors (11). In our study six independent MD simulations were performed. All initial PDE$\delta$ coordinate files were retrieved from available x-ray crystal structures, which were solved by Zimmermann et al. (11). These x-ray structures show co-crystallized ligands bound to the active site (Fig. 1).

PDE$\delta$ has a large binding pocket, which has mainly two essential regions. Compounds **2** and **5** have extensive structures and can be localized in these two regions. However, compounds **1** and **S1** have relatively small sizes and can be localized in either the first or second regions. (In our study, we called these regions 1 and 2 at the binding pocket, which are near the Tyr149 and Arg61 key amino acid residues, respectively). To check the structural effects of the inhibitors **1** and **S1** in both regions, we performed MD simulations in the two regions individually for these inhibitors. To illustrate the most likely pose of the inhibitors from the ensemble generated by MD simulations in a single snapshot, the average structures were calculated and used for root mean-square deviation (RMSD) fitting. The frame with the coordinates closest to the average structure (i.e., RMSD values are calculated in respect to the average conformer for each frame) was selected as a representative snapshot from whole 7000 frames, which are derived from 70 ns MD simulations.

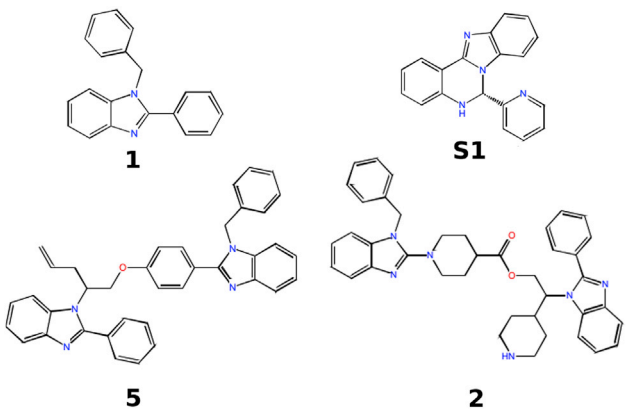


FIGURE 1 Chemical structures of novel inhibitors (co-crystallized) used in this study.

Fig. 2 shows the representative structures of ligands **2** and **5** during MD simulations. Their coordinates at the active site are superimposed with coordinates of the co-crystallized ligands. Distinct poses are not observed between the co-crystallized and representative ligands from MD simulations in the PDE$\delta$ active site for both ligands. This indicates a high stability of the inhibitors at the binding pocket.

Two-dimensional ligand interaction diagrams are profiled for compounds **2** and **5**, which show interactions of compounds within 4 Å distance threshold (see Fig. S2). As Fig. S2 clearly shows, Arg61 and Tyr149 established H-bonding interactions with compounds **2** and **5**. Also strong $\pi$-$\pi$ stacking interactions are formed with Trp32 for both ligands. These extended ligands cover overall binding pocket of the PDE$\delta$ as shown in Fig. 2.

## Hydrogen bond occupancy analysis and per-residue interaction energy estimations

To understand the H-bonding population of each inhibitor during simulation with key amino acid residues of the PDE$\delta$, H-bond analysis were performed independently for each inhibitor. The percentage of H-bond occupancy during simulations was calculated for studied six different systems and plotted in Fig. 3.

These profile shows valuable information of the H-bonding network during inhibitory treatment. The inhibitor **5** constructs a diverse H-bonding network at the binding pocket with several key amino acids such as Tyr149, Arg61, Val145, Met118, and Leu38. This may explain inhibitor **5's** strong inhibitory profile (10 nM). Ligand **1** in two different active site positions (i.e., $\mathbf{1_1}$ and $\mathbf{1_2}$) formed different H-bonding interactions. PDE$\delta$ involves a single extended binding cavity at the x-ray structure that includes both Arg61 and Tyr149 amino acids. Compounds **1** and **S1** at region 1 ($1_1$ and $S1_1$) formed H-bonds with Tyr149 with the occupancy of 28% and 75%, respectively. These inhibitors at region 2 ($1_2$ and $S1_2$) constructed H-bonds mainly with Arg61 with the occupancy of 50.45% and 56.55%, respectively. Moreover, per-residue interaction energy analysis were obtained between individual amino acid residues-inhibitor interactions as shown in Fig. 4.

Arg61 was indicated as a key residue for ligand interaction for all inhibitors except ligands $\mathbf{1_1}$ and $\mathbf{S1_1}$, as expected.

## Binding enthalpies from the MM-PBSA/GBSA computations

To estimate binding free energies of the four different inhibitors with PDE$\delta$, both MM-PBSA and MM-GBSA methods were used. The analysis of binding thermodynamics for the six complexes is shown in Table 1. The free-energy decomposition to individual components illustrates the impact of each energy contribution to the binding affinity of the

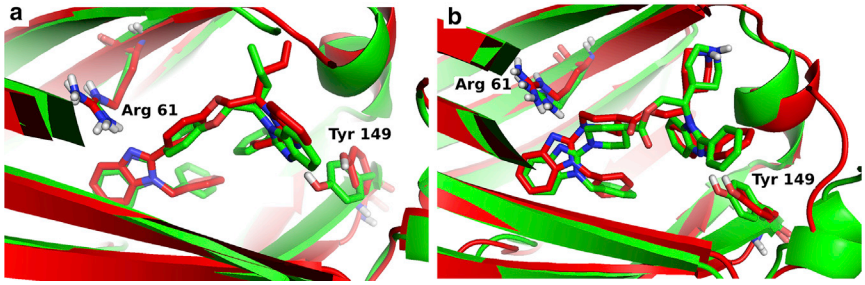


FIGURE 2 Structural superposition of crystallized PDE$\delta$ enzyme (*green*) with equilibrated K-RAS via MD simulations (*red*). Interacted with ligands 2 (*a*) and 5 (*b*).

receptor to various ligands. In all complex formations, the computed binding enthalpies overestimate the experimental results. Nevertheless, the binding enthalpies are positively correlated with the measured affinities.

Table 1 includes results of binding enthalpy estimations using MM-PBSA/GBSA calculations for all studied systems. The experimental binding affinity values of bound ligands toward PDE$\delta$ reported by Zimmermann et al. (11) and their converted $\Delta G$ values are also listed in the Table 1. Parallel to the experimental results, MM-PBSA/GBSA analysis showed that inhibitor **5** has the most strongly bounded ligand at the active site (Table 1). The compound **2** has the second-highest inhibitory activity based on our predictions and experimental results. For compounds **1** and **S1**, energetic estimations of the four complex formations were individually examined. As described in Materials and Methods, these ligands are small in size; therefore, the two independent ligand-binding pockets of the receptor were studied and also the average binding energy of both pockets were accurately considered. The ligand **1** revealed an absolute higher binding free energy compared with ligand **S1** in the first binding pocket of the PDE$\delta$. However, the ligand **S1** displayed higher predicted affinity to the second binding site. The binding enthalpy differences between the first and second binding pockets were calculated for ligand **1** and ligand **S1** (Table 1). Both inhibitors have theoretically shared the similar binding energy values. There was no significant difference between the binding energies of both ligands according experimental results ($\Delta G_{exp}$ of ligands **1** and **S1** are $-9.30$ and $-8.02$ kcal/mole, respectively). In addition to the free-energy differences, other individual energy components were also derived, such as van der Waals, electrostatic, polar solvation, nonpolar solvation, and MM interaction energies. These results illustrate that van der Waals and electrostatic interaction energies are treated favorably by the binding sites of all complexes. Particularly, these energy components within the PDE$\delta$ in complex with inhibitors **2** and **5** are amply pronounced, because of the fact that ligands **2** and **5** are more extended in size in comparison with other inhibitors (**1** and **S1**).

## Stability and clustering analysis

Conformational clustering analyses were also performed for the studied inhibitors during MD simulations. Fig. 5 clearly illustrates the evolution of the conformational transitions for each inhibitor in various positions in the course of MD simulations.

RMSD calculations of heavy atoms were carried out on the six ligands to examine the conformational stability of the inhibitor in the active site of PDE$\delta$ during the simulation (Fig. S3). Ligand $\mathbf{1_1}$ was more unstable compared with the other inhibitors throughout the simulation. Inhibitor **5** fluctuated less than other compounds as expected. To understand the influence of each inhibitor to overall PDE$\delta$ structure, root-mean-square fluctuation (RMSF) calculations were also applied (Fig. 6).

The average flexibility of individual amino acid residues in respect to the six ligands bound was plotted. The lowest amino acids fluctuations were found for inhibitors **5** and **2**.

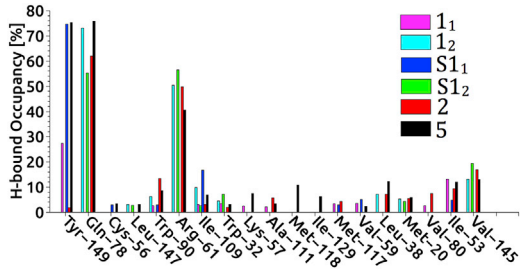


FIGURE 3 The occupancy of the hydrogen bond between protein and ligands.

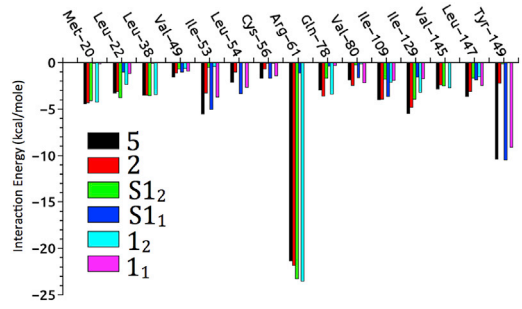


FIGURE 4 The nonbonded interaction energy analysis between residues in the active site and ligands.

**TABLE 1 Energetic analysis for PDE$\delta$ complexes as obtained by MM-GBSA/PBSA calculations**

| Energy (kcal/mole) | $1_1$ | $1_2$ | $1_1$ and $1_2$ | $S1_1$ | $S1_2$ | $S1_1$ and $S1_2$ | 2 | 5 |
|---|---|---|---|---|---|---|---|---|
| $\Delta E_{vdw}$ | −41.88 ± 2.10 | −38.87 ± 2.36 | −40.37 | −38.96 ± 2.14 | −41.82 ± 2.34 | −40.39 | −79.51 ± 3.43 | −76.19 ± 3.37 |
| $\Delta E_{elec}$ | −3.57 ± 1.21 | −4.46 ± 2.36 | −4.01 | −3.55 ± 1.87 | −4.37 ± 1.63 | −3.96 | −84.63 ± 13.06 | −11.89 ± 1.71 |
| $\Delta E_{MM}$ | −45.45 ± 2.47 | −43.34 ± 2.72 | −44.39 | −42.51 ± 2.83 | −46.19 ± 3.17 | −44.35 | −164.15 ± 13.64 | −88.09 ± 3.75 |
| $\Delta G_{p\ (gb)}$ | 10.82 ± 1.30 | 10.71 ± 1.52 | 10.76 | 12.83 ± 1.96 | 10.57 ± 1.36 | 11.7 | 102.05 ± 12.03 | 22.90 ± 1.49 |
| $\Delta G_{np\ (gb)}$ | −5.25 ± 0.17 | −5.35 ± 0.22 | −5.30 | −4.95 ± 0.20 | −5.44 ± 0.18 | −5.19 | −10.39 ± 0.30 | −10.19 ± 0.28 |
| $\Delta G_{solv}$ | 5.57 ± 1.32 | 5.36 ± 1.55 | 5.36 | 7.87 ± 1.90 | 5.12 ± 1.29 | 6.49 | 91.66 ± 12.02 | 12.71 ± 1.49 |
| $\Delta G_{elec(tot)}$[a] | 7.25 | 6.25 | 6.75 | 9.28 | 6.2 | 7.74 | 17.42 | 11.01 |
| $\Delta G_{MM\text{-}GBSA}$ | −39.89 ± 2.16 | −37.99 ± 2.30 | −38.94 | −34.65 ± 2.33 | −41.07 ± 2.63 | −37.86 | −72.50 ± 4.02 | −75.39 ± 3.77 |
| $\Delta G_{MM\text{-}PBSA}$ | −32.37 ± 2.41 | −29.72 ± 2.56 | −31.04 | −29.48 ± 2.82 | −32.76 ± 2.75 | −31.2 | −58.66 ± 4.45 | −59.25 ± 3.74 |
| $K_{D\ exp}$ (nM) | 165 ± 23 | 165 ± 23 | | 1420 ± 480 | 1420 ± 480 | | 39 ± 11 | 10 ± 3 |
| $\Delta G_{exp}$ | −9.30 | | | −8.02 | | | −10.16 | −10.97 |

50 ns MD simulations were carried out for all the systems using AMBER.
[a]$\Delta G_{elec\ (tot)} = \Delta G_{elec} + \Delta G_{p\ (gb)}$.

The less-stable protein structure during simulation was found for ligand $\mathbf{1_1}$.

## Cardiotoxicity

One of the most common side effects reported for a number of diverse small molecules is their off-target interactions with cardiac ion channels especially with hERG K channels. Thus, all of these novel, to our knowledge, PDE$\delta$ inhibitors were also screened in silico at the central cavities of model hERG1 channels using our previously developed hERG1 open and open-inactivated S1–S6 TM domains (28). In the derivation of these channel models, available experimental constraints were used (29-31). All six novel inhibitors were docked into the active site of two models of hERG1, and the calculated docking score values are listed in Table S1.

Three-dimensional and two-dimensional docking poses of ligands **1** and **2** are displayed in Figs. S4 and S5, respectively. Our simulations results show that all novel inhibitors have high docking scores at open inactivated hERG1 models. Therefore, our molecular simulations suggest that rehabilitation of these inhibitors is needed before further biological tests can be undertaken.

## CONCLUSIONS

In summary, we have performed six long-range independent classic MD simulations. To investigate the mechanistic inhibitory treatment of PDE$\delta$ bound to novel various inhibitors, different postprocessing MD analyses were carried out. In this article, we reported on the capacity of each inhibitor to cover the active site of PDE$\delta$ protein and also on the stability of inhibitors by means of RMSD, RMSF, and clustering analysis approaches at the binding site. In addition, we also carried out binding enthalpy estimation studies of ligands. To the best of our knowledge, this study is one of the first in silico investigation of the PDE$\delta$ protein. A detailed atomic scale understanding of molecular mechanism of PDE$\delta$ inhibition may assist in the design and development of novel and more potent PDE$\delta$ inhibitors.

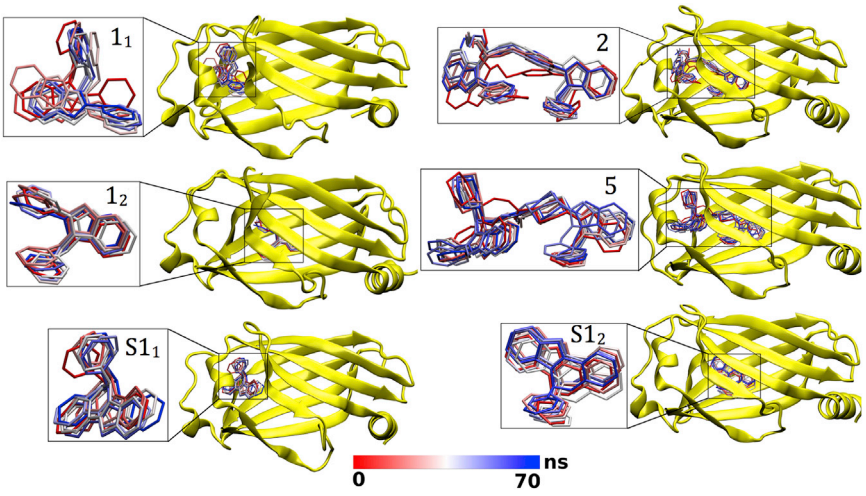


FIGURE 5 Illustrative structures of the studied ligand conformations in PDE$\delta$ protein using clustering analysis.

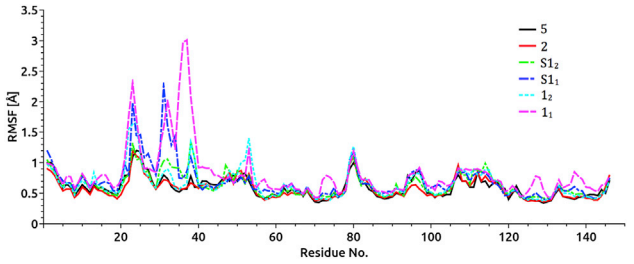


FIGURE 6 The root-mean-square fluctuation (RMSF) values calculated from the 70 ns MD trajectories for all inhibitor complexed with PDE$\delta$ protein are displayed versus the residue number.

## SUPPORTING MATERIAL

Five figures and one table are available at http://www.biophysj.org/biophysj/supplemental/S0006-3495(15)00781-X.

## AUTHOR CONTRIBUTIONS

S.D. designed the experiments. R.E.S., M.M., and S.D. carried out the experiments. R.E.S., S.D., S.N., and M.Y. analyzed and discussed the results. R.E.S. prepared figures. R.E.S., M.Y., S.N, and S.D. wrote the manuscript.

## REFERENCES


1. Hirakawa, T., and H. E. Ruley. 1988. Rescue of cells from ras oncogene-induced growth arrest by a second, complementing, oncogene. *Proc. Natl. Acad. Sci. USA.* 85:1519–1523.
2. Harvey, J. J. 1964. An unidentified virus which causes the rapid production of tumours in mice. *Nature.* 204:1104–1105.
3. Ellis, C. A., and G. Clark. 2000. The importance of being K-Ras. *Cell. Signal.* 12:425–434.
4. Jančík, S., J. Drábek, …, D. Radzioch. 2010. Clinical relevance of KRAS in human cancers. *J. Biomed. Biotechnol.* 2010:150960.
5. Bell, D. A. 2005. Origins and molecular pathology of ovarian cancer. *Mod. Pathol.* 18 (*Suppl. 2*):S19–S32.
6. Carta, C., F. Pantaleoni, …, M. Tartaglia. 2006. Germline missense mutations affecting KRAS isoform B are associated with a severe Noonan syndrome phenotype. *Am. J. Hum. Genet.* 79:129–135.
7. Birchenall-Roberts, M. C., T. Fu, …, F. W. Ruscetti. 2006. K-Ras4B proteins are expressed in the nucleolus: interaction with nucleolin. *Biochem. Biophys. Res. Commun.* 348:540–549.
8. Bos, J. L. 1989. *ras* oncogenes in human cancer: a review. *Cancer Res.* 49:4682–4689.
9. Dmitrovsky, E., V. V. Murty, …, R. S. Chaganti. 1990. Isochromosome 12p in non-seminoma cell lines: karyologic amplification of c-ki-ras2 without point-mutational activation. *Oncogene.* 5:543–548.
10. Welman, A., M. M. Burger, and J. Hagmann. 2000. Structure and function of the C-terminal hypervariable region of K-Ras4B in plasma membrane targetting and transformation. *Oncogene.* 19:4582–4591.
11. Zimmermann, G., B. Papke, …, H. Waldmann. 2013. Small molecule inhibition of the KRAS-PDE$\delta$ interaction impairs oncogenic KRAS signalling. *Nature.* 497:638–642.
12. Eswar, N., D. Eramian, …, A. Sali. 2008. Protein structure modeling with MODELLER. *Methods Mol. Biol.* 426:145–159.
13. Pettersen, E. F., T. D. Goddard, …, T. E. Ferrin. 2004. UCSF Chimera—a visualization system for exploratory research and analysis. *J. Comput. Chem.* 25:1605–1612.
14. Boutet, E., D. Lieberherr, …, A. Bairoch. 2007. UniProtKB/Swiss-Prot. *Methods Mol. Biol.* 406:89–112.
15. Bas, D. C., D. M. Rogers, and J. H. Jensen. 2008. Very fast prediction and rationalization of pKa values for protein-ligand complexes. *Proteins.* 73:765–783.
16. Sastry, G. M., M. Adzhigirey, …, W. Sherman. 2013. Protein and ligand preparation: parameters, protocols, and influence on virtual screening enrichments. *J. Comput. Aided Mol. Des.* 27:221–234.
17. Kalé, L., R. Skeel, …, K. Schulten. 1999. NAMD2: greater scalability for parallel molecular dynamics. *J. Comput. Phys.* 151:283–312.
18. MacKerell, A. D., D. Bashford, …, M. Karplus. 1998. All-atom empirical potential for molecular modeling and dynamics studies of proteins. *J. Phys. Chem. B.* 102:3586–3616.
19. Vanommeslaeghe, K., E. Hatcher, …, A. D. Mackerell, Jr. 2010. CHARMM general force field: a force field for drug-like molecules compatible with the CHARMM all-atom additive biological force fields. *J. Comput. Chem.* 31:671–690.
20. Humphrey, W., A. Dalke, and K. Schulten. 1996. VMD: visual molecular dynamics. *J. Mol. Graph.* 14:33–38.
21. Case, D. A., T. E. Cheatham, 3rd, …, R. J. Woods. 2005. The Amber biomolecular simulation programs. *J. Comput. Chem.* 26:1668–1688.
22. Hornak, V., R. Abel, …, C. Simmerling. 2006. Comparison of multiple Amber force fields and development of improved protein backbone parameters. *Proteins.* 65:712–725.
23. Wang, J., R. M. Wolf, …, D. A. Case. 2004. Development and testing of a general Amber force field. *J. Comput. Chem.* 25:1157–1174.
24. Miller, B. R., T. D. McGee, …, A. E. Roitberg. 2012. *MMPBSA.py*: an efficient program for end-state free energy calculations. *J. Chem. Theory Comput.* 8:3314–3321.
25. Weiser, J. J., P. S. Shenkin, and W. C. Still. 1999. Approximate atomic surfaces from linear combinations of pairwise overlaps (LCPO). *J. Comput. Chem.* 20:217–230.
26. Sanguinetti, M. C., and M. Tristani-Firouzi. 2006. hERG potassium channels and cardiac arrhythmia. *Nature.* 440:463–469.
27. Halgren, T. A., R. B. Murphy, …, J. L. Banks. 2004. Glide: a new approach for rapid, accurate docking and scoring. 2. Enrichment factors in database screening. *J. Med. Chem.* 47:1750–1759.
28. Durdagi, S., S. Deshpande, …, S. Y. Noskov. 2012. Modeling of open, closed, and open-inactivated states of the hERG1 channel: structural mechanisms of the state-dependent drug binding. *J. Chem. Inf. Model.* 52:2760–2774.
29. Zhang, M., J. Liu, …, G. N. Tseng. 2005. Interactions between charged residues in the transmembrane segments of the voltage-sensing domain in the hERG channel. *J. Membr. Biol.* 207:169–181.
30. Tristani-Firouzi, M., J. Chen, and M. C. Sanguinetti. 2002. Interactions between S4-S5 linker and S6 transmembrane domain modulate gating of HERG K+ channels. *J. Biol. Chem.* 277:18994–19000.
31. Tseng, G. N., K. D. Sonawane, …, H. R. Guy. 2007. Probing the outer mouth structure of the HERG channel with peptide toxin footprinting and molecular modeling. *Biophys. J.* 92:3524–3540.